Progress In Electromagnetics Research C, Vol. 103, 83–95, 2020

Fields of an Ultra-Relativistic Beam of Charged Particles between Parallel Plates. Exact Two-Dimensional Solutions by the Method of Images and Applications to the HL-LHC

Boris B. Levchenko*

Abstract—Exact two-dimensional (2D) analytic expressions for electric and magnetic fields and their potentials created by a linear beam of relativistic charged particles between infinite perfectly conductive plates and ferromagnetic poles are derived. The solutions are obtained by summing an infinite sequence of fields from linear charge-images and current-images in complex space. Knowledge of the normal component of the electric field on the conductor surface makes it possible to calculate the induced electric charge surface density. In addition, we derive within an improved linear approximation new analytical expressions for fields near the beam in the case of an arbitrary beam offset from the median plane. The mathematical features of exact solutions and limitations for the applicability of linear approximations are specified. The primary goals of the future high-luminosity *p*-*p* and heavy-ion Large Hadron Collider programme after the Long Shutdown 2 are the search for yet unobserved effects of physics beyond the Standard Model, searches for rare or low-sensitivity processes in the Higgs sector, and probing in more detail the mechanism of electroweak symmetry breaking. This programme relies on the stable operation of the accelerator. However, as the beam luminosity increases, a number of destabilizing phenomena occur, in particular field emission, enhancing the electron cloud effect. For the case of a proton beam, we apply the exact 2D solution for estimating the intensity of electron field emission activated by the electric field of the beam in collimators of the future high-luminosity Large Hadron Collider. Calculation shows that the field emission intensity is very sensitive to a collimator surface roughness. In addition, with a relatively small and accidental beam displacement from the median path, about 20% of the collimator half-gap, the emission intensity increases by a factor of 10^7. This will partially neutralize the beam space charge, violating acceleration dynamics, and enhancing instability effects.

1. INTRODUCTION

The external electric field $\mathbf{E}$ and magnetic induction $\mathbf{B}$ of a beam of relativistic charged particles with a uniform linear density and circular cross section are described by expressions (see Refs. [1] (Section 18.2.4) and [2])

$$\mathbf{E}_{\rm dir} = \frac{2\kappa\lambda}{r}\frac{\mathbf{r}}{r}, \quad \mathbf{B}_{\rm dir} = \frac{1}{c}\boldsymbol{\beta}\times\mathbf{E}, \tag{1}$$

where $\kappa = 1/4\pi\epsilon_0$, λ is the linear beam density with account the particle charge, $\boldsymbol{\beta} = \mathbf{v}/c$ a normalized velocity vector of the beam constituents, and c the velocity of light. The radius vector $\mathbf{r}$ is perpendicular to the velocity vector.

Received 29 March 2020, Accepted 10 June 2020, Scheduled 21 June 2020
* Corresponding author: Boris B. Levchenko (levtchen@mail.desy.de).
The author is with the D.V. Skobeltsyn Institute of Nuclear Physics, M.V. Lomonosov Moscow State University, Moscow 119991, Russian Federation.

If the beam is surrounded by conducting and ferromagnetic surfaces (as in charged particle accelerators), then the fields around the beam change.† To account for these changes, there is a relatively simple method developed by William Thomson (Lord Kelvin) [3] and described in much detail in the Maxwell treatise [4], referred to as the method of mirror charges and currents or the method of images. For example, with the use of this method in [5] for the first time 1D projections E_y and B_x of fields were calculated when generated by a cylindrical beam between infinitely wide parallel ideally conducting plates, and/or between ferromagnetic parallel poles. Both types of planes are parallel and symmetrical to the coordinate plane (x, z). However, an infinite sequence of fields from image charges and image currents were summed up only in the linear approximation in y and $\bar{y}$, the coordinate of the field observation point on the y-axis, $(0, y)$ and the beam offset from the origin, respectively.

As a result, due to presence of the parallel conducting and ferromagnetic plates, additional induced fields arise near the beam

$$\mathrm{E}_{y,\,\mathrm{im}}(y,\bar{y}) = \frac{4\kappa\lambda}{h^2}\,\epsilon_1(y+2\bar{y}), \quad \mathrm{B}_{x,\,\mathrm{im}}(y,\bar{y}) = \frac{2\kappa\lambda\beta}{cg^2}\,\epsilon_2(2y+\bar{y}). \tag{2}$$

Here h and g are half-gaps between the conducting plates and between the poles of magnets, correspondingly. The coefficients $\epsilon_1 = \pi^2/48$ and $\epsilon_2 = \pi^2/24$ are called the Laslett form factors for infinite parallel plate vacuum chambers and magnetic poles, respectively. The truncated linear approximation Eq. (2) is widespread in textbooks, reference books and lectures (see, for example, [1, 6, 7]).‡ Conditions for the applicability of this linear approximation are violated if the observation point of the field y is located far off the beam, and if the center of a beam $\bar{y}$ is far shifted toward the conducting surface.

The exact solution of this one dimensional problem by the method of images was presented by the author in [2, 8],

$$\mathrm{E}_{y,\,\mathrm{im}}(\delta,\bar{\delta}) = \frac{4\kappa\lambda}{h}\,\Lambda(\delta,\bar{\delta}), \quad \mathrm{B}_{x,\,\mathrm{im}}(\eta,\bar{\eta}) = \frac{4\kappa\lambda\beta}{gc}H(\eta,\bar{\eta}), \tag{3}$$

where the structural functions of the fields are of the form

$$\begin{aligned}
\Lambda(\delta,\bar{\delta}) &= \frac{1}{2}\left\{\frac{\pi}{4}\tan\left[\frac{\pi}{4}\left(\delta+\bar{\delta}\right)\right] + \frac{\pi}{4}\cot\left[\frac{\pi}{4}\left(\delta-\bar{\delta}\right)\right] - \frac{1}{\delta-\bar{\delta}}\right\},\\
H(\eta,\bar{\eta}) &= \frac{1}{2}\left\{\frac{\pi}{4}\tan\left[\frac{\pi}{4}\left(\eta+\bar{\eta}\right)\right] - \frac{\pi}{4}\cot\left[\frac{\pi}{4}\left(\eta-\bar{\eta}\right)\right] + \frac{1}{\eta-\bar{\eta}}\right\}.
\end{aligned} \tag{4}$$

The variables, $\delta = y/h$, $\bar{\delta} = \bar{y}/h$, $\eta = y/g$, $\bar{\eta} = \bar{y}/g$ correspond to the scaled y and $\bar{y}$ coordinates. By expanding trigonometric functions into series, one can obtain both approximations in Eq. (2) and the full linear approximations, including generalized form factors $\epsilon_1(\bar{\delta})$, $\epsilon_1(\bar{\eta})$, valid for arbitrary $\bar{\delta}$ and $\bar{\eta}$ [2]. The complete linear approximations are important in the study of dynamics of particles near the beam and the beam itself with a significant deviation from the median plane [2].

The representation of a vacuum chamber and magnetic poles in the form of infinite parallel plates is a very useful mathematical abstraction. However, in real accelerators, all components are finite although some of these components include elements which are structurally designed as parallel conductive and ferromagnetic flat surfaces. In circular accelerators such as LHC [9] and the future HL-LHC [10], flat parallel surfaces are parts of different types of collimators, the normal conducting separator and orbit correction dipole magnets.§ As a rule, collimator jaws have a length of 600–1400 mm, and their width is about 90 mm, with a jaw flatness of about 40 μm along the 1 m long active jaw surface. Similarly, the poles of a dipole magnet have a length of 2000–3400 mm and a pole width of 60 mm [10]. With transverse beam sizes as small as 200 μm, the representation of collimators and dipole magnets in the form of infinite parallel plates is a good approximation for these elements and it is therefore legitimate to apply results obtained here in various applications.

† In the following, we distinguish between the fields created by the beam itself, i.e., own, direct fields (with the index "dir") and fields from induced charges and currents (with the index "im").

‡ We understand under the complete linear approximation an expression linear in y, but summed up in all orders of $\bar{y}$.

§ A list of collimators for the LHC Run 2 (in 2015) includes 108 items and shown on p. 151 of the technical design report "High-Luminosity Large Hadron Collider (HL-LHC)" [10].

To calculate the particle trajectories in the halo of the beam or the evolution of electrons emitted from the jaws of a collimator, it is necessary to know the 2D distribution of fields in the gap between the plates.[‖] All these problems are relevant for the HL-LHC under construction [11] and discussed partly in Section 6. In the following sections we present exact 2D solutions for the fields $\mathbf{E}_{\rm im}$ and $\mathbf{B}_{\rm im}$ obtained by the method of image charges and currents.

2. 2D ELECTRIC FIELD FROM IMAGE-CHARGES

Let us calculate the field $\mathbf{E}_{\rm im}$ in the space between perfectly conducting parallel infinite plates, when the particle beam moves parallel to the plates. Let us direct the z-axis of the right-handed Cartesian coordinate system (x, y, z) along the velocity vector of the beam particles, and also direct the y-axis perpendicular to the conducting plates. The plates themselves will be placed at a distance $y = \pm h$ from the origin. Then the x-axis will be perpendicular to the beam and lies in the median plane between the plates. Suppose that the constituents of the beam are positively charged. For example, it can be a beam of protons or ions. By construction, our problem is two-dimensional and static and, therefore, it is necessary to calculate the field components only in the x-y plane. For full generality, let the beam center be displaced to the point $(\bar{x}, \bar{y})$, and the observation point of the field be at (x, y) between conducting parallel plates. This is shown in Figure 1.

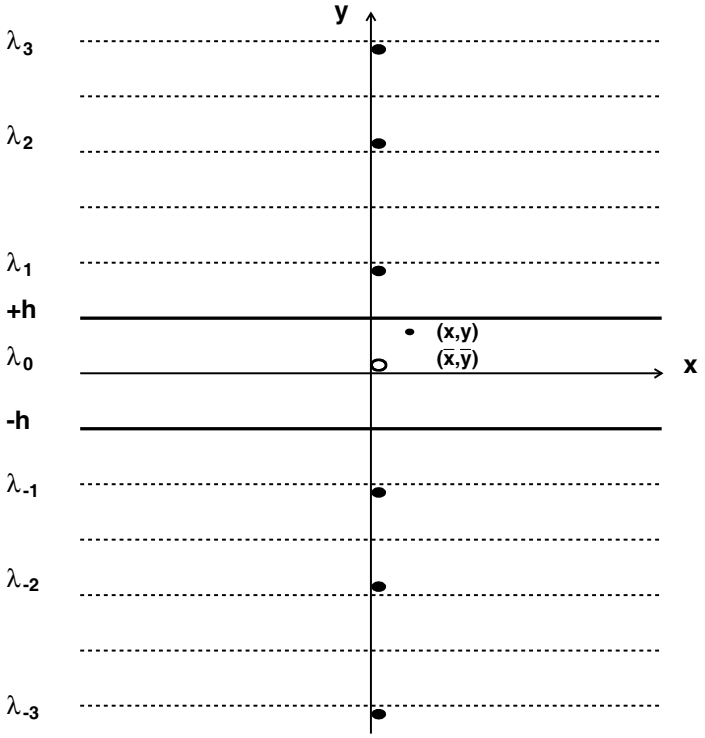

Figure 1. The electric field in the point (x, y) between conducting plates $y = \pm h$ is generated by the direct source-charge λ_0 at $(\bar{x}, \bar{y})$ (the direct field) and the successive image charges $\lambda_{\pm i}$ at locations $(\bar{x}, d_{\pm k})$ and $(\bar{x}, d_{\pm m})$ (see explanation in text).

The boundary condition on the x-component of the electric field on the surface of perfectly conducting plates is $E_x(x, \pm h) = 0$ (equipotential surfaces) and is satisfied if image charges change sign from image to image.

A test charged particle placed at a point (x, y) is affected by both the direct field from the source-

[‖] A study of QED effects in the beam fields will be presented elsewhere.

charge λ_0 and the fields of all image charges $\lambda_{\pm i}$ For instance, charges[¶] λ_1 and λ_{-1} are generated by λ_0 due to reflection in plates $+h$ and $-h$, respectively. The charges λ_2 and λ_{-2} are generated by λ_{-1} and λ_1 due to reflection in plates $+h$ and $-h$, respectively, and so on. With the help of Figure 1, one can easily calculate y-coordinates of all image charges. So, for odd images, $k = 1, 3, 5, ...$, the differences of y-coordinates between $\lambda_{\pm k}$ and the observation point y are $d_{\pm k} = 2kh \mp y_+$. For even images, $m = 2, 4, 6, ...$, the differences of y-coordinates between $\lambda_{\pm m}$ and the observation point y are $d_{\pm m} = 2mh \mp y_-$. Here, $y_+ = y + \bar{y}$ and $y_- = y - \bar{y}$.

The successful solution of the 1D problem was because the distance between the field points was determined by a simple difference in coordinates, and the need to summarize a series of elementary fractions [2]. In the 2D problem, a distance is already specified through a power function. The transition to the potential greatly facilitates the solution of electrostatic problems.

In the complex z-plane, $z = x + iy$, we define the field by $\mathrm{E}(z) = -\partial\Phi/\partial z$. If we set the complex potential of the beam with a linear charge density λ as $\Phi(z - \bar{z}) = -2\kappa\lambda \ln(z - \bar{z})$ then the complex field of such a beam is $\mathrm{E}(z) = 2\kappa\lambda/(z - \bar{z})$. Thus, in the components, the direct beam field is

$$\mathrm{E}_{\mathrm{dir}}(z) = \frac{2\kappa\lambda}{|r - \bar{r}|} \cdot \frac{x - \bar{x}}{|r - \bar{r}|} - i\frac{2\kappa\lambda}{|r - \bar{r}|} \cdot \frac{y - \bar{y}}{|r - \bar{r}|} = \mathrm{E}_{x,\,\mathrm{dir}} - i\mathrm{E}_{y,\,\mathrm{dir}}. \tag{5}$$

Let us compose the sum of the potentials from the first-level images λ_1 and λ_{-1} (Figure 1),

$$\begin{aligned}\Phi_1 &= -2\kappa\lambda\left[(-1)\ln(z - z_1) + (-1)\ln(z - z_{-1})\right] \\ &= 2\kappa\lambda\left\{\ln[x - \bar{x} + i(y_+ - 2h)] + \ln\left[x - \bar{x} + i(y_+ + 2h)\right]\right\} = 2\kappa\lambda\ln[\hat{z}_+^2 + (2h)^2],\end{aligned} \tag{6}$$

with $\hat{z}_+ = x - \bar{x} + iy_+$. For an arbitrary odd $k = 2n + 1$,

$$\Phi_k = 2\kappa\lambda\ln[\hat{z}_+^2 + (2kh)^2] = 2\kappa\lambda\ln\left\{(2kh)^2\left[1 + \frac{(\hat{z}_+/2h)^2}{(2n+1)^2}\right]\right\}. \tag{7}$$

The sum of potentials from images with even m, λ_m and λ_{-m}, is

$$\begin{aligned}\Phi_m &= -2\kappa\lambda\left\{\ln[x - \bar{x} + i(y_- - 2mh)] + \ln[x - \bar{x} + i(y_- + 2mh)]\right\} \\ &= -2\kappa\lambda\ln\left\{(2mh)^2\left[1 + \frac{(\hat{z}_-/2h)^2}{(2n+2)^2}\right]\right\},\end{aligned} \tag{8}$$

where $\hat{z}_- = x - \bar{x} + iy_-$. The resulting potential is $\Phi_{\mathrm{im}} = \sum_k \Phi_k + \sum_m \Phi_m$,

$$\Phi_{\mathrm{im}}(\hat{z}_+, \hat{z}_-) = 2\kappa\lambda\left[\ln\frac{\prod_{n=0}^{\infty}(2n+1)^2}{\prod_{n=0}^{\infty}(2n+2)^2} + \ln\prod_{n=0}^{\infty}\left(1 + \frac{(\hat{z}_+/2h)^2}{(2n+1)^2}\right) - \ln\prod_{n=0}^{\infty}\left(1 + \frac{(\hat{z}_-/2h)^2}{(2n+2)^2}\right)\right]. \tag{9}$$

In calculating the field components, the first constant term does not contribute.

We apply now the representation of hyperbolic functions in the form of infinite products and transform Eq. (9) to the following form

$$\Phi_{\mathrm{im}}(\hat{z}_+, \hat{z}_-) = 2\kappa\lambda\Big\{\ln[\cosh(\hat{\delta}_+)] - \ln[\sinh(\hat{\delta}_-)] + \ln\hat{\delta}_-\Big\}, \tag{10}$$

where $\hat{\delta}_+ = \pi\hat{z}_+/4h$ and $\hat{\delta}_- = \pi\hat{z}_-/4h$.

In the old textbook [12], a similar problem for the electrostatic field was solved by the method of conformal mapping. Only the electrostatic field potential was calculated. The expressions for the potential coincide with Eq. (10) if $a = 2h$ and $b = h + \bar{y}$ are used in formula (3), Section 4.20 of [12], and normalised variables are not used.

We find an expression for the complex field of electrical images by differentiating the complex potential (10) with respect to z,

$$\mathrm{E}_{\mathrm{im}}(z) = \frac{2\kappa\lambda}{h}\frac{\pi}{4}\left[\coth(\hat{\delta}_-) - \tanh(\hat{\delta}_+) - \frac{1}{\hat{\delta}_-}\right]. \tag{11}$$

[¶] Below, for short, instead of the term "charge-image", we will write "charge".

The real components of the electric field, $E_{x,\,\mathrm{im}}$ and $E_{y,\,\mathrm{im}}$, in accordance with the definition in Eq. (5), are

$$\mathrm{E}_{x,\,\mathrm{im}} = -\mathrm{Re}\frac{\partial \Phi_{\mathrm{im}}}{\partial z}, \quad \mathrm{E}_{y,\,\mathrm{im}} = \mathrm{Im}\frac{\partial \Phi_{\mathrm{im}}}{\partial z}. \tag{12}$$

Let us introduce the scaled coordinates of the field observation point, $\delta_x = x/h$, $\delta_y = y/h$, the scaled coordinates of the beam position, $\bar{\delta}_x = \bar{x}/h$, $\bar{\delta}_y = \bar{y}/h$ and also variables $\Delta_x = \delta_x - \bar{\delta}_x$, $\Delta_{y-} = \delta_y - \bar{\delta}_y$, $\Delta_{y+} = \delta_y + \bar{\delta}_y$. After simple but long algebraic transformations, we get the following formulas for components of the resulting image field,

$$\begin{aligned}
\mathrm{E}_{x,\,\mathrm{im}}(x,y) \;=\; & \frac{2\kappa\lambda}{h}\frac{\pi}{8}\frac{\sinh\left(\frac{\pi}{2}\Delta_x\right)\cos\left(\frac{\pi}{2}\delta_y\right)\cos\left(\frac{\pi}{2}\bar{\delta}_y\right)}{\left[\sinh^2\left(\frac{\pi}{4}\Delta_x\right)+\cos^2\left(\frac{\pi}{4}\Delta_{y+}\right)\right]\left[\sinh^2\left(\frac{\pi}{4}\Delta_x\right)+\sin^2\left(\frac{\pi}{4}\Delta_{y-}\right)\right]} \\
& -\frac{2\kappa\lambda}{h}\frac{\Delta_x}{\Delta_x^2+\Delta_{y-}^2},
\end{aligned} \tag{13}$$

$$\begin{aligned}
\mathrm{E}_{y,\,\mathrm{im}}(x,y) \;=\; & \frac{2\kappa\lambda}{h}\frac{\pi}{8}\left\{\frac{\sin\left(\frac{\pi}{2}\Delta_{y+}\right)}{\sinh^2\left(\frac{\pi}{4}\Delta_x\right)+\cos^2\left(\frac{\pi}{4}\Delta_{y+}\right)}+\frac{\sin(\frac{\pi}{2}\Delta_{y-})}{\sinh^2\left(\frac{\pi}{4}\Delta_x\right)+\sin^2\left(\frac{\pi}{4}\Delta_{y-}\right)}\right\} \\
& -\frac{2\kappa\lambda}{h}\frac{\Delta_{y-}}{\Delta_x^2+\Delta_{y-}^2}.
\end{aligned} \tag{14}$$

To obtain the complete distribution of the electric field between the conducting plates and to meet the boundary condition that the electric field enters conducting surfaces perpendicularly, image fields $\mathbf{E}_{\mathrm{im}}$ must be added to the direct field of the beam,

$$\mathrm{E}_{x,\,\mathrm{dir}}(x,y) = \frac{2\kappa\lambda}{h}\frac{\Delta_x}{\Delta_x^2+\Delta_{y-}^2}, \quad \mathrm{E}_{y,\,\mathrm{dir}}(x,y) = \frac{2\kappa\lambda}{h}\frac{\Delta_{y-}}{\Delta_x^2+\Delta_{y-}^2}. \tag{15}$$

It is interesting to note some features of Eqs. (13) and (14). First, the coordinates of the field observation point enters only via the scaled variables. In addition, the last terms in Eqs. (13) and (14) have signs opposite to those of the components of the direct field of the beam, Eq. (15). Adding the components of Eqs. (13), (14), and (15), we find the total field to be

$$\begin{aligned}
\mathrm{E}_{x,\,\mathrm{tot}}(\delta_x,\delta_y,\bar{\delta_x},\bar{\delta_y}) \;=\; & \frac{2\kappa\lambda}{h}\frac{\pi}{8}\frac{\sinh\left[\frac{\pi}{2}(\delta_x-\bar{\delta}_x)\right]}{\left[\sinh^2\left[\frac{\pi}{4}(\delta_x-\bar{\delta}_x)\right]+\cos^2\left[\frac{\pi}{4}(\delta_y+\bar{\delta_y})\right]\right]} \\
& \times\frac{\cos\left(\frac{\pi}{2}\delta_y\right)\cos\left(\frac{\pi}{2}\bar{\delta_y}\right)}{\left[\sinh^2\left[\frac{\pi}{4}(\delta_x-\bar{\delta}_x)\right]+\sin^2\left[\frac{\pi}{4}(\delta_y-\bar{\delta_y})\right]\right]},
\end{aligned} \tag{16}$$

$$\begin{aligned}
\mathrm{E}_{y,\,\mathrm{tot}}(\delta_x,\delta_y,\bar{\delta_x},\bar{\delta_y}) \;=\; & \frac{2\kappa\lambda}{h}\frac{\pi}{8}\left\{\frac{\sin\left[\frac{\pi}{2}(\delta_y+\bar{\delta_y})\right]}{\sinh^2\left[\frac{\pi}{4}(\delta_x-\bar{\delta}_x)\right]+\cos^2\left[\frac{\pi}{4}(\delta_y+\bar{\delta_y})\right]}\right. \\
& \left.+\frac{\sin\left[\frac{\pi}{2}(\delta_y-\bar{\delta_y})\right]}{\sinh^2\left[\frac{\pi}{4}(\delta_x-\bar{\delta}_x)\right]+\sin^2\left[\frac{\pi}{4}(\delta_y-\bar{\delta_y})\right]}\right\}.
\end{aligned} \tag{17}$$

A direct verification shows that Eq. (16) satisfies the boundary condition $\mathrm{E}_{x,\,\mathrm{tot}}(\delta_x,\pm 1,\bar{\delta_x},\bar{\delta_y}) = 0$ and in the 1D limit, $\delta_x = \bar{\delta_x} = 0$ and $\mathrm{E}_{x,\,\mathrm{tot}} = 0$. Similarly, Eq. (14) at $\delta_x = \bar{\delta_x} = 0$ goes into Eq. (3), with $\delta = \delta_y$ and $\bar{\delta} = \bar{\delta_y}$. In particular, a beam moving in the midplane generates the field described by

$$E_{y,\,\mathrm{tot}}(\delta_x,\delta_y,0,0) = \frac{2\kappa\lambda}{h}\frac{\pi}{8}\frac{\sin\left(\frac{\pi}{2}\,\delta_y\right)\left[1+2\sinh^2\left(\frac{\pi}{4}\,\delta_x\right)\right]}{\left[\sinh^2\left(\frac{\pi}{4}\,\delta_x\right)+\sin^2\left(\frac{\pi}{4}\,\delta_y\right)\right]\left[\sinh^2\left(\frac{\pi}{4}\,\delta_x\right)+\cos^2\left(\frac{\pi}{4}\,\delta_y\right)\right]}.$$

In other words, in the presence of conducting plates the electric field in front of the plate, $\delta_y = 1$, $\delta_x = 0$ is enhanced by the factor $\pi/2$.

3. 2D MAGNETIC FIELD FROM IMAGE-CURRENTS

In the above, we have discussed electric image fields created by an ultra-relativistic beam. Magnetic images can be treated in much the same way. Let the ferromagnetic boundaries be represented by a pair of infinitely wide parallel plates at $y = \pm g$. On the surface of a ferromagnetic with a very high magnetic permeability ($\mu \to \infty$), only the normal component $\mathbf{B}$ is nonzero. This boundary condition is satisfied if the image currents have the same direction as the beam current.

From Eq. (1), the components of $\mathbf{B}$, given that $\mathrm{v}_x = \mathrm{v}_y = 0$ and $\mathrm{v}_z = \mathrm{v}$, are

$$\mathrm{B}_x = -\beta \mathrm{E}_y/c, \quad \mathrm{B}_y = \beta \mathrm{E}_x/c. \tag{18}$$

With the use of the relationship (18), we apply now the method of complex potential, as in the previous section. After self-evident replacements in Eq. (7) and (8), we obtain an analogue of (10),

$$\Psi_{\mathrm{im}}(\hat{\eta}_+, \hat{\eta}_-) = -2\kappa\lambda(\beta/c)\Big\{ \ln[\cosh(\hat{\eta}_+)] + \ln[\sinh(\hat{\eta}_-)] - \ln \hat{\eta}_- \Big\}, \tag{19}$$

where $\hat{\eta}_+ = \pi \hat{z}_+/4g$ and $\hat{\eta}_- = \pi \hat{z}_-/4g$ are normalized to the half-gap g between ferromagnetic poles. For the resulting complex magnetic induction from image currents, we find

$$\mathrm{B}_{\mathrm{im}}(z) = \frac{2\kappa\lambda\beta}{gc}\frac{\pi}{4}\left[\tanh(\hat{\eta}_+) + \coth(\hat{\eta}_-) - \frac{1}{\hat{\eta}_-}\right]. \tag{20}$$

Components of the magnetic induction vector are calculated by $\mathrm{B}_{x,\,\mathrm{im}} = -\mathrm{Im}\,\partial\Psi_{\mathrm{im}}/\partial z$, $\mathrm{B}_{y,\,\mathrm{im}} = -\mathrm{Re}\,\partial\Psi_{\mathrm{im}}/\partial z$, or directly from Eq. (20). In order to obtain the complete distribution of the magnetic field between the ferromagnetic plates and fulfil the boundary condition on the plates, it is necessary to add the field $\mathbf{B}_{\mathrm{im}}$ to the self-field of the beam. As previously for the electric field, adding each component $\mathrm{B}_{x,\,\mathrm{im}}$, $\mathrm{B}_{y,\,\mathrm{im}}$ and $\mathrm{B}_{x,\,\mathrm{dir}}$, $\mathrm{B}_{y,\,\mathrm{dir}}$, we find the components of the vector of total magnetic induction

$$\begin{aligned}
\mathrm{B}_{x,\,\mathrm{tot}}(\eta_x, \eta_y, \bar{\eta}_x, \bar{\eta}_y) \;=\; & \frac{\kappa\pi\lambda\beta}{4gc}\left\{ \frac{\sin\left[\frac{\pi}{2}(\eta_y + \bar{\eta}_y)\right]}{\sinh^2\left[\frac{\pi}{4}(\eta_x - \bar{\eta}_x)\right] + \cos^2\left[\frac{\pi}{4}(\eta_y + \bar{\eta}_y)\right]} \right. \\
& \left. - \frac{\sin\left[\frac{\pi}{2}(\eta_y - \bar{\eta}_y)\right]}{\sinh^2\left[\frac{\pi}{4}(\eta_x - \bar{\eta}_x)\right] + \sin^2\left[\frac{\pi}{4}(\eta_y - \bar{\eta}_y)\right]} \right\},
\end{aligned} \tag{21}$$

$$\begin{aligned}
\mathrm{B}_{y,\,\mathrm{tot}}(\eta_x, \eta_y, \bar{\eta}_x, \bar{\eta}_y) \;=\; & \frac{\kappa\pi\lambda\beta}{4gc}\left\{ \frac{\sinh\left[\frac{\pi}{2}(\eta_x - \bar{\eta}_x)\right]}{\sinh^2\left[\frac{\pi}{4}(\eta_x - \bar{\eta}_x)\right] + \cos^2\left[\frac{\pi}{4}(\eta_y + \bar{\eta}_y)\right]} \right. \\
& \left. + \frac{\sinh\left[\frac{\pi}{2}(\eta_x - \bar{\eta}_x)\right]}{\sinh^2\left[\frac{\pi}{4}(\eta_x - \bar{\eta}_x)\right] + \sin^2\left[\frac{\pi}{4}(\eta_y - \bar{\eta}_y)\right]} \right\},
\end{aligned} \tag{22}$$

where $\eta_x = x/g$, $\bar{\eta}_x = \bar{x}/g$, $\eta_y = y/g$, $\bar{\eta}_y = \bar{y}/g$.

Directly from Eq. (21) it is difficult to see that at $\eta_y = \pm 1$ the boundary condition $\mathrm{B}_{x,\,\mathrm{tot}}(\eta_x, \pm 1, \bar{\eta}_x, \bar{\eta}_y) = 0$ is satisfied. However, it can be verified that $\mathrm{B}_{x,\,\mathrm{tot}} \sim \cos(\pi\eta_y/2)$, and thus the specified boundary condition is indeed satisfied.

4. SURFACE CHARGE DENSITY

The distribution of the charge density σ induced by a beam on the surface of a conductor is determined by the normal component E_n of the electric field at a given point on the surface. For our problem,

$\mathrm{E}_n = -\mathrm{E}_{y,\,\mathrm{tot}}(\delta_x, \pm 1, \bar{\delta}_x, \bar{\delta}_y)$. The charge distributions σ are different on the upper, $\delta_y = +1$, and lower, $\delta_y = -1$, plates. Thus, according to the Gauss-Ostrogradsky theorem,

$$\sigma_{\pm 1}\left(\delta_x, \bar{\delta}_x, \bar{\delta}_y\right) = -\epsilon_0 \mathrm{E}_{y,\,\mathrm{tot}}\left(\delta_x, \pm 1, \bar{\delta}_x, \bar{\delta}_y\right), \tag{23}$$

where $\mathrm{E}_{y,\,\mathrm{tot}}$ is given by Eq. (17).

5. LINEAR APPROXIMATIONS FOR IMAGE FIELDS

An interesting mathematical feature of the exact functions $\Lambda(\delta, \bar{\delta})$ and $H(\eta, \bar{\eta})$ from Eq. (3) was noted in [2]. This is a kind of permutation symmetry that connects the components of the fields $\mathrm{E}_{y,\,\mathrm{im}}$ and $\mathrm{B}_{x,\,\mathrm{im}}$. This functional symmetry is obvious from Eq. (4): $H(\eta, \bar{\eta}) = \Lambda(\bar{\eta}, \eta)$. In 2D solutions, Eqs. (17) and (21), the functional parts of formulas retain this symmetry, as is directly verified. This symmetry is also present in Eq. (2).

It is quite time-consuming to derive the linear approximation for the components of $\mathbf{E}_{\mathrm{im}}(x, y)$ directly from Eqs. (16), (17). The result is achieved faster with the use of the complex form Eq. (11). Let us decompose the function of two variables $\mathrm{E}_{\mathrm{im}}(z)$ in a series near the point $(\bar{x}, \bar{y})$ and keep the terms linear in $x - \bar{x}$ and $y - \bar{y}$. However, when decomposing $\coth(\hat{\delta}_-)$, we have to account the presence of a singular term, $\coth(\hat{\delta}_-) \approx \hat{\delta}_-^{-1} + \hat{\delta}_-/3 + \cdots$. Thus,

$$\mathrm{E}_{\mathrm{im}}(z) \approx -\frac{4\kappa\lambda}{h}\left\{\epsilon_1(\bar{\delta}_y)[(\delta_x - \bar{\delta}_x) + i(\delta_y - \bar{\delta}_y)] + i\frac{\pi}{8}\tan\left(\frac{\pi}{2}\bar{\delta}_y\right)\right\}, \tag{24}$$

or, in accordance with Eq. (5),

$$\mathrm{E}_{x,\,\mathrm{im}} \approx -\frac{4\kappa\lambda}{h}\,\epsilon_1(\bar{\delta}_y)(\delta_x - \bar{\delta}_x), \quad \mathrm{E}_{y,\,\mathrm{im}} \approx \frac{4\kappa\lambda}{h}\Big[\frac{\pi}{8}\tan\left(\frac{\pi}{2}\,\bar{\delta}_y\right) + \epsilon_1(\bar{\delta}_y)(\delta_y - \bar{\delta}_y)\Big]. \tag{25}$$

Here we have introduced [2] a generalization of the Laslett electric image coefficient ϵ_1 in the case of an arbitrary beam offset $\bar{\delta}_y$,

$$\epsilon_1(\bar{\delta}_y) = \frac{\pi^2}{32}\left[\frac{1}{\cos^2\left(\frac{\pi}{2}\bar{\delta}_y\right)} - \frac{1}{3}\right], \quad \epsilon_1(0) = \frac{\pi^2}{48}. \tag{26}$$

Thus, the vertical component of the electric field in the vicinity of the plate, $|\bar{\delta}_y| \sim 1$, $|\delta_y - \bar{\delta}_y| \ll 1$ is given by

$$E_{y,\,\mathrm{tot}}(0, \delta_y, 0, \bar{\delta}_y) \approx \frac{2\kappa\lambda(z,t)}{h}\left[\frac{1}{\delta_y - \bar{\delta}_y} + \frac{\pi}{4}\frac{1}{\cos\left(\frac{\pi}{2}\,\bar{\delta}_y\right)} + \frac{\pi^2}{16}\frac{(\delta_y - \bar{\delta}_y)}{\cos^2\left(\frac{\pi}{2}\,\bar{\delta}_y\right)}\right]. \tag{27}$$

Here we only retained the main singular contributions. Eq. (27) tell us that with an increase of $\bar{\delta}_y$ the field strength near the plate significantly increase due to images and under the influence of the Lorentz force the beam is attracted by the conducting plate.

Usually [1, 7], after solving a 1D problem and finding $\mathrm{E}_{y,\,\mathrm{im}}$ of the form Eq. (2), to find the second component of the field, $\mathrm{E}_{x,\,\mathrm{im}}$, one use the following condition that the components of the image fields must satisfy,

$$\boldsymbol{\nabla}\mathbf{E}_{\mathrm{im}} = \frac{\partial \mathrm{E}_{x,\,\mathrm{im}}}{\partial x} + \frac{\partial \mathrm{E}_{y,\,\mathrm{im}}}{\partial y} = 0. \tag{28}$$

It is easy to verify that the field projections in Eq. (25) satisfy the condition in Eq. (28).

Now we calculate in a linear approximation the components of the magnetic induction vector. For this, we also use the complex representation of Eq. (20). Repeating the expansion of the hyperbolic functions in a series, as in the calculation of E_{im}, we obtain

$$\mathrm{B}_{x,\,\mathrm{im}} \approx \frac{4\kappa\lambda\beta}{gc}\Big[\frac{\pi}{8}\tan\left(\frac{\pi}{2}\bar{\eta}_y\right) + \epsilon_2(\bar{\eta}_y)(\eta_y - \bar{\eta}_y)\Big], \quad \mathrm{B}_{y,\,\mathrm{im}} \approx \frac{4\kappa\lambda\beta}{gc}\epsilon_2(\bar{\eta}_y)(\eta_x - \bar{\eta}_x). \tag{29}$$

Here we have introduced [2, 13] a generalization of the Laslett form factor for infinite parallel plate magnet poles ϵ_2 in the case of an arbitrary offset $\bar{\eta}_y$,

$$\epsilon_2(\bar{\eta}_y) = \frac{\pi^2}{32}\left[\frac{1}{\cos^2\left(\frac{\pi}{2}\bar{\eta}_y\right)} + \frac{1}{3}\right], \quad \epsilon_2(0) = \frac{\pi^2}{24}. \tag{30}$$

In order to illustrate the accuracy of the linear approximations in Eqs. (2) and (29) we construct ratios, R, of the exact solution $\mathrm{B}_{x,\,\mathrm{im}}$ from Eq. (21) to $\mathrm{B}_{x,\,\mathrm{im}}$ from Eq. (2) and to $\mathrm{B}_{x,\mathrm{im}}$ from Eq. (29). Figure 2 shows these ratios at three values of $\bar{\eta}_y$. We conclude that in contrast to Eq. (2), the linear approximations in Eq. (29) properly take into account the dependence on $\bar{\eta}_y$ but the range of applicability of the modified linear approximation shrinks with an increase of $\bar{\eta}_y$.

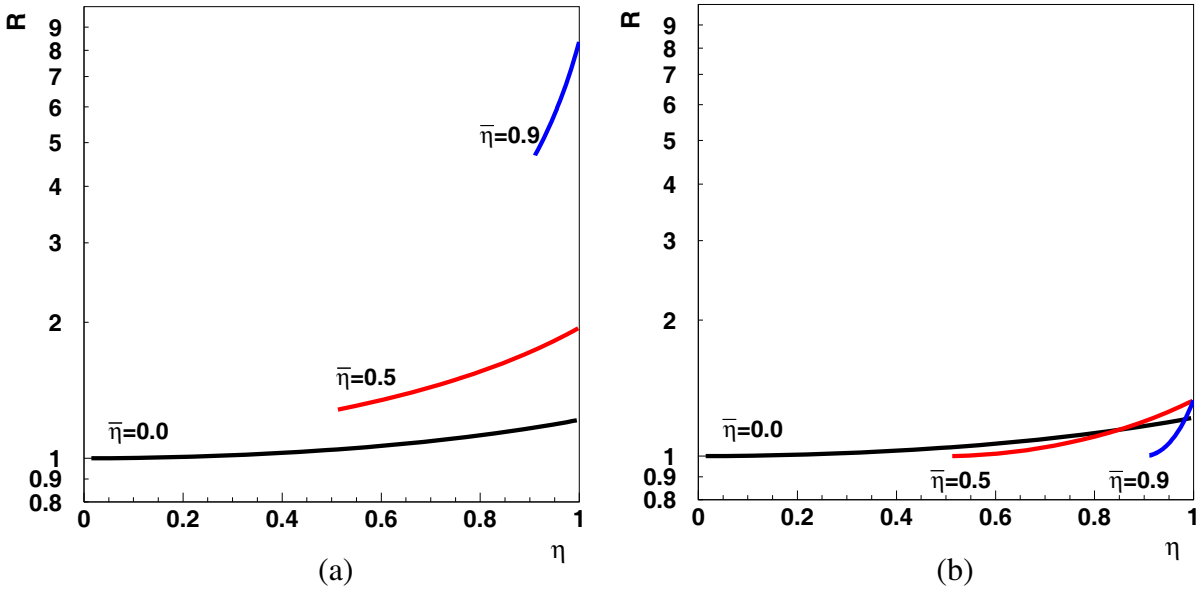

Figure 2. Comparison of linear approximations for the magnetic induction of image fields with the exact solution at three values of the beam offset $\bar{\eta}$: (a) The ratio of $\mathrm{B}_{x,\,\mathrm{im}}$ from Eq. (21) to $\mathrm{B}_{x,\,\mathrm{im}}$ from Eq. (2); (b) The ratio of $\mathrm{B}_{x,\,\mathrm{im}}$ from Eq. (21) to $\mathrm{B}_{x,\,\mathrm{im}}$ from Eq. (29).

In conclusion, it should be noted that the condition in Eq. (28) is not a universal way to recover the missing field component. Indeed, if one starts with "a wrong component", say, only the component $\mathrm{E}_{x,\,\mathrm{im}}$ is known, then it is possible to restore $\mathrm{E}_{y,\,\mathrm{im}}$ only up to an unknown constant C. There are no additional conditions to restore this constant in the form $\mathrm{C} = \frac{\pi}{8}\tan\left(\frac{\pi}{2}\bar{\delta}_y\right)$.

Another limitation of the applicability of the linear approximation near the conductor surface, both Eq. (2) and improved Eq. (25), is the violation of the boundary condition $\mathrm{E}_{x,\,\mathrm{tot}} = \mathrm{E}_{x,\,\mathrm{im}} + \mathrm{E}_{x,\,\mathrm{dir}} = 0$ at $\delta_y = \pm 1$. The same applies to the component $\mathrm{B}_{x,\,\mathrm{im}}$ in Eq. (29): $\mathrm{B}_{x,\,\mathrm{tot}} \neq 0$ at $\eta_y = \pm 1$. The permutation symmetry mentioned at the beginning of the section for the exact expressions of the components $\mathrm{E}_{y,\,\mathrm{im}}$ and $\mathrm{B}_{x,\,\mathrm{im}}$ is lost in the linear approximations of Eqs. (25) and (29).

6. FIELD EMISSION FROM JAWS OF A HL-LHC COLLIMATOR

The transverse beam profile in an accelerator is formed not only by the magnetic system, but also by collimators, absorbing the halo of the beam, and protecting other parts of the accelerator in case of beam instability. As noted in Section 1, the HL-LHC beam diameter, $2\sigma_x$, is much smaller than the width of the collimator jaws and less than the working distance between the plates. The surfaces of collimators are made of electrically conductive alloys, resistant to high temperature and a mechanical

stress. An ultra-relativistic beam of charged particles is the source of a strong electric field. It is in the collimator that the beam is closest to the electrically conductive surfaces. As a result of these factors, the electron field emission occurs from surfaces of a collimator[+]. Once in the channel of the accelerator, these electrons generate a whole chain of processes that affect the stability of the high-energy beam. Accelerated by the electric field of the beam, electrons begin to collide with the walls of the vacuum chamber, knock out additional electrons and emit bremsstrahlung photons, thereby leading to cascade multiplication of the number of electrons [14]. An increasing number of electrons leads to partial neutralization of the beam space charge, violating acceleration dynamics, and enhancing the effects of instability. A summary of the Fowler-Nordheim theory of field emission is presented in Appendix A.

In modern accelerators, the beam splits into bunches. Here we consider bunches shaped as a cylinder of length L_b with a circular cross section. The coordinate z-axis is along the bunch velocity vector. The space-time distribution of the electric field around an ultra-relativistic circular bunch with a uniform particle density is described by a step-like form [2]:

$$\mathbf{E}(r,z,t) = \frac{2\kappa\lambda}{r}\frac{\mathbf{r}}{r}\Big[\theta(z-\beta ct) - \theta(z-\beta ct - L_b)\Big]. \tag{31}$$

This field contains only the radial component and in the functional sense at every moment coincides with the field of a continuous beam (1). For this reason, formulae derived in Sections 2 and 3 for fields of a continuous beam between parallel plates are also applicable for calculating fields of an ultra-relativistic bunch [2].

We apply Eq. (17) and formulae from Appendix A for evaluating the effective field emission current and the electron emission intensity from the jaw surface in one of the HL-LHC collimators. The emission current density $\mathbf{J}$ depends not only on the magnitude of the electric field on the surface, but also on the morphological features of the conductor surface that can locally significantly strengthen the applied electric field. The deviation of the real surface (with microscopic protrusions, apexes, scratches) from a perfectly smooth surface is characterized by the field enhancement factor $\beta_{FN} \geq 1$. For a particular surface, an average $\bar{\beta}_{FN}$ is determined by measurements. Collimators with working surfaces made of different materials (CFC, MoGr, Mo) are under study for the HL-LHC [10]. Based on the surface photos of collimator prototypes [10], we consider that the field enhancement $\bar{\beta}_{FN}$ can reach a value of several tens of units.

For numerical calculations we use the HL-LHC proton beam parameters ([10], Table 2-1) and parameters of a TCSMP/TCTPM collimator with a molybdenum surface ([10], Tables 5-3, 5-4). Figure 3(a) shows the distribution of electric field intensity on a jaw surface. The number of electrons per second emitted from the collimator jaws is

$$N_e(\beta_{FN}) = n_b N_r \sum \iiint \frac{1}{e}\mathbf{J}(\beta_{FN}\mathrm{E}_y)\Theta(z,t)\mathrm{d}x\mathrm{d}z\mathrm{d}t. \tag{32}$$

Here, the integration is carried out over the emission area $S(t)$ activated on the jaw of length L_j by the field pulse from a bunch of length L_b. The function $\Theta(z,t)$ is the step-like part of Eq. (31). The emission is summed from both jaws. The duration of the field pulse is $\Delta t = L_j/c$. It is necessary to take into account that in the HL-LHC proton beam there will be $n_b = 2748$ bunches and per second the beam makes $N_r = 11245$ revolutions. Appendix B gives details of calculating N_e by Equation (32).

Figure 3(b) shows the results of calculating $N_e(\beta_{FN})$ for different values of h and $\bar{\delta}_y$. So, in the scenario C, at $\beta_{FN} \sim 80$ the number of electrons emitted per second already exceeds the number of protons in one bunch, $N_p = 2.2 \cdot 10^{11}$. And with a certain shift of the beam from the midplane (scenario D, $\bar{\delta}_y = 0.2$), the number of emitted electrons increases by four orders of magnitude and exceeds the total number of protons in the beam, the order of $6.0 \cdot 10^{14}$. It should be noted that our estimations does not take into account contributions from other collimators, the dynamical multiplication of the number of electrons during rescattering, as well as electron absorption in other parts of the accelerator, for instance, in a special beam screen.

[+] Levchenko, B. B., "On field emission in high energy colliders initiated by a relativistic positively charged bunch of particles," arXiv:physics/0608135, 1–28, 2006.

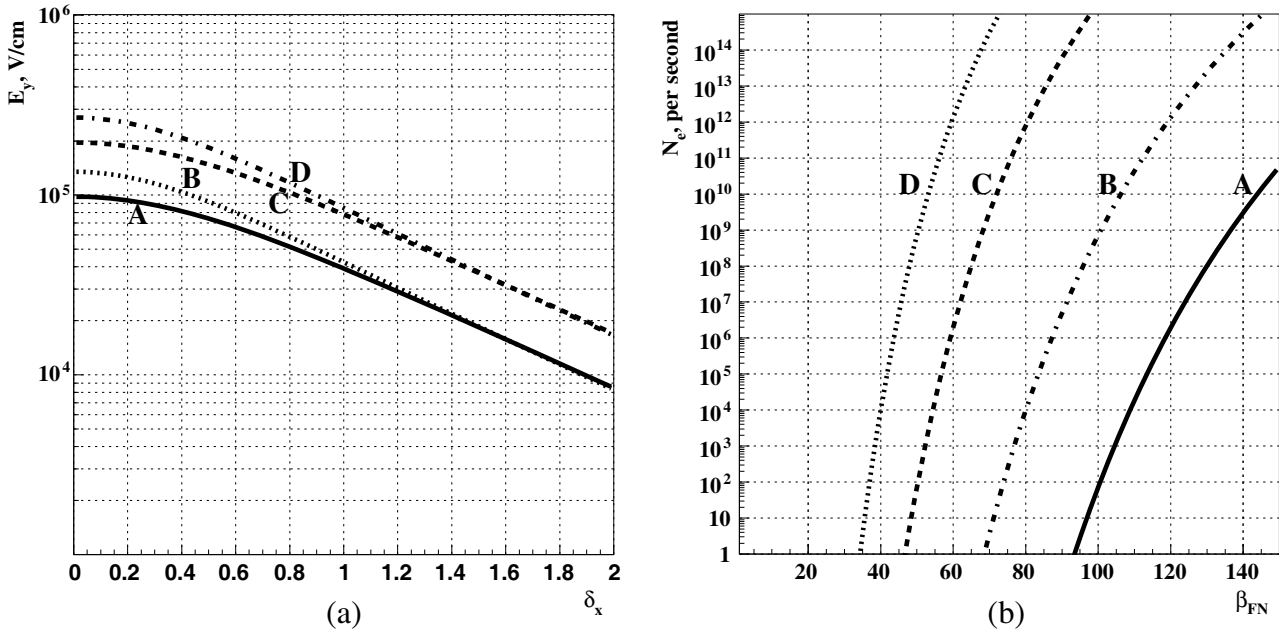

Figure 3. (a) The electric field strength profile at a collimator jaw surface as a function of the scaled x-coordinate. (b) The electron emission intensity from a molybdenum-coated collimator as a function of β_{FN}. Calculations are performed for different scenarios of jaw opening h and the beam displacement from the midplane $\bar{\delta}_y$: A — $2h = 1\,\text{mm}$, $\bar{\delta}_y = 0$; B — $2h = 1\,\text{mm}$, $\bar{\delta}_y = 0.2$; C — $2h = 0.5\,\text{mm}$, $\bar{\delta}_y = 0.0$; D — $2h = 0.5\,\text{mm}$, $\bar{\delta}_y = 0.2$. Other parameters are as follows [10]: number protons per bunch $N_p = 2.2 \cdot 10^{11}$, $L_b = \sqrt{2\pi}\sigma_z = 20.3\,\text{cm}$, with σ_z denoting the r.m.s. bunch length, $\varphi_{Mo} = 4.27\,\text{eV}$, $L_j = 100\,\text{cm}$, $T = 327\,\text{K}$.

7. SUMMARY

We analyzed the problem of summing up the fields of the images generated by a charged beam between infinitely wide parallel conducting plates and/or ferromagnetic poles. The new exact 2D solutions for resulting electric and magnetic fields are represented in terms of elementary trigonometric and hyperbolic functions. The expressions for modified fields are applied to develop improved linear approximations for image fields and to generalize the Laslett image coefficients to the case of an arbitrary beam offset. We apply the solution for the electric field between parallel conducting plates to calculate the surface distribution of the induced electric charge and for evaluating the electron emission intensity from a molybdenum-coated collimator of the future HL-LHC. To conclude, we note the need "to certify" the jaw surface of all collimators by the value of $\bar{\beta}_{FN}$ and simulate the particle beam wiring throughout the accelerator to determine optimal working distances between jaws from minimizing the field emission.

ACKNOWLEDGMENT

The author is grateful to M. Wing for reading the manuscript, questions and comments and E. B. Oborneva for discussions.

APPENDIX A. FIELD EMISSION IN A STRONG ELECTRIC FIELD

This summary of the Fowler-Nordheim theory of field emission is based on the review* and Refs. [15–26].

* Levchenko, B. B., "On field emission in high energy colliders initiated by a relativistic positively charged bunch of particles," 1–28, arXiv:physics/0608135, 2006.

A.1. Fowler-Nordheim Theory

In the framework of Fowler-Nordheim (F-N) theory, the current density of field emission of electrons from a metal can be written in the following form

$$\mathbf{J}_{FN} = e \int n(\mathcal{E}_y) D(\mathcal{E}_y, \mathrm{E}_y) d\mathcal{E}_y, \tag{A1}$$

where $D(\mathcal{E}_y, \mathrm{E}_y)$ is the penetration coefficient, and $n(\mathcal{E}_y)$ is the number of electrons at the energy $\mathcal{E}_y$ incident in the y-direction on the surface barrier from inside of the metal.

An electron outside a metal is attracted to the metal as a result of the charge it induces on the surface (image force). In the externally applied accelerating electric field E_y, the potential energy of the electron is

$$V(y) = -\frac{e^2}{4y} - e\mathrm{E}_y y, \quad \text{when } y > 0, \tag{A2}$$

where y denotes the distance from the surface and the first term accounts for the image potential[♯]. With use of the potential energy in Eq. (A2) and the Fermi energy distribution of electrons in the conduction band, one finds that

$$\mathbf{J}_{FN}(\mathrm{E}_y) = A\frac{{\mathrm{E}_y}^2}{\varphi \cdot t^2(\tau)} \exp\Big\{ - B\frac{\varphi^{3/2}}{\mathrm{E}_y}\vartheta(\tau)\Big\}, \tag{A3}$$

where $\mathbf{J}$ is the current density in A/cm^2, E_y the electric field on the surface in V/cm, and φ the work function in eV. The field-independent constants A and B and the variable τ are

$$\begin{aligned} A &= \frac{e^3}{8\pi h} = 1.5414 \cdot 10^{-6}, \quad B = \frac{8\pi\sqrt{2m}}{3eh} = 6.8309 \cdot 10^7, \\ \tau &= \frac{\sqrt{e^3\mathrm{E}_y}}{\varphi} = 3.7947 \cdot 10^{-4}\frac{\sqrt{\mathrm{E}_y}}{\varphi}, \end{aligned} \tag{A4}$$

where $-e$ is the charge on the electron, m the electron mass, and h the Planck's constant. The numerical values of A and B correspond to values of the physical constants [27]. We note that under field emission conditions, $0 < \tau \leq 1$.

The Nordheim function $\vartheta(\tau)$ takes into account a lowering of the potential barrier due to the image potential (the Schottky effect) and its distinction from an idealized triangular shape. The function $t(\tau)$ in the denominator of Eq. (A3) is defined as

$$t(\tau) = \vartheta(\tau) - (2\tau/3)(d\vartheta/d\tau). \tag{A5}$$

The function $\vartheta(\tau)$ varies from $\vartheta(0) = 1$ to $\vartheta(1) = 0$ with the increase in field strength, however $t(\tau)$ is quite close to unity at all values of τ.

For a typical metallic φ of 4.5 eV, fields of the order of 10^7 V/cm are needed to have measurable emission currents. In considering magnitudes, one must always keep in mind the rapid variation of the exponential function. For instance, an increase in E of only a factor of two from 1×10^7 to 2×10^7 V/cm increases the current density by 15 orders of magnitude (from 10^{-18} to 10^{-3} A/cm^2)!

At a field strength of the order of $\mathrm{E}_{cr} = \varphi^2/e^3 = 6.945 \cdot 10^6 \cdot \varphi^2$ V/cm, the height of the potential barrier vanishes and $\vartheta(1) = 0$. For instance, for copper $\varphi_{Cu} = 4.65$ eV giving $\mathrm{E}_{cr}(Cu) = 1.5 \cdot 10^8$ V/cm, and similarly for graphite, $\varphi_{gr} = 4.6$ eV, $\mathrm{E}_{cr}(gr) = 1.47 \cdot 10^8$ V/cm. At this field level one would expect the orderly bound states characteristic of the solid to lose their integrity.

For a long time only tabulated values of $\vartheta(\tau)$ and $t(\tau)$ [28] were used in calculations, see [21–26]. Several parameterizations of functions $\vartheta(\tau)$ and $t(\tau)$ were proposed[††].

The theory of field emission from metals has been subjected to fairly extensive verification. A variety of methods have been employed over many years for the experimental measurements of the emission current as a function of the field strength, the work function and the energy distribution of the emitted electrons [23–26]. The F-N theory (A3) of electron emission from plane and uniform metal surfaces (single-crystal plane) at $T \approx 0$ may therefore be considered well established experimentally as well as on theoretical grounds.

[♯] In this section we adopt the Gaussian CGS system.

[††] Levchenko, B. B., "On parameterizations of the Nordheim functions," arXiv:cond-mat/0512513, 2005.

A.2. Temperature Dependence

The main Equation (A3) of the F-N theory was derived for an idealized metal in the framework of the Sommerfeld model, with an ideally flat surface and at a very low temperature, $T \approx 0$. The temperature dependence of the field emission current (FEC) is completely connected with the change of the spectrum of electrons in the metal with an increase in T. Therefore, at non-zero temperatures the F-N theory must be modified to take into account the thermal excitation of electrons above the Fermi level. For the so-called extended field emission region, Murphy and Good [21] obtained the following elegant equation

$$\mathbf{J}_{FN}(\mathrm{E}_y, T) = \frac{\pi\omega}{\sin\pi\omega}\mathbf{J}_{FN}(\mathrm{E}_y, 0), \tag{A6}$$

which accounts for the temperature dependence of the FEC. Here $\omega = k_B T/k_B T_0$ and

$$k_B T_0 = \frac{2}{3}\frac{\mathrm{E}_y}{Bt(\tau)\sqrt{\varphi}}, \tag{A7}$$

where k_B is Boltzmann's constant, and T is the absolute temperature in K. It can be shown [21] that Eq. (A6) is a valid approximation when the following two conditions are satisfied:

$$\omega < \left[1 + \frac{1}{\Gamma_1}\right]^{-1}, \quad \Gamma_1 = \frac{\varphi(1-\tau)}{k_B T_0} - \frac{2}{\pi}\left(\frac{2}{\tau}\right)^{1/2} t(\tau), \tag{A8}$$

and

$$\omega < \left[1 + \frac{1}{\Gamma_2}\right]^{-1}, \quad \Gamma_2 \simeq \left(\frac{2\varphi}{k_B T_0 t(\tau)}\right)^{1/2}. \tag{A9}$$

At very low temperatures, when $\pi\omega$ is small, Eq. (A6) reduces to Eq. (A3). By expanding $\sin\pi\omega$ in a series, one gets for practical use the formula

$$\mathbf{J}_{FN}(\mathrm{E}_y, T)/\mathbf{J}_{FN}(\mathrm{E}_y, 0) = 1 + 1.40 \cdot 10^8 (\varphi/\mathrm{E}_y^2) T^2. \tag{A10}$$

It is easy to estimate using Eq. (A10) that for $\varphi = 4.5\,\mathrm{eV}$ at room temperature, $T = 300\,\mathrm{K}$, and the field strength $\mathrm{E}_y = 1 \times 10^7\,\mathrm{V/cm}$ and $2 \times 10^7\,\mathrm{V/cm}$. The temperature factor in Eq. (A6) equals 1.57 and 1.14, respectively. Thus, the temperature factor appear to be a sizeable correction.

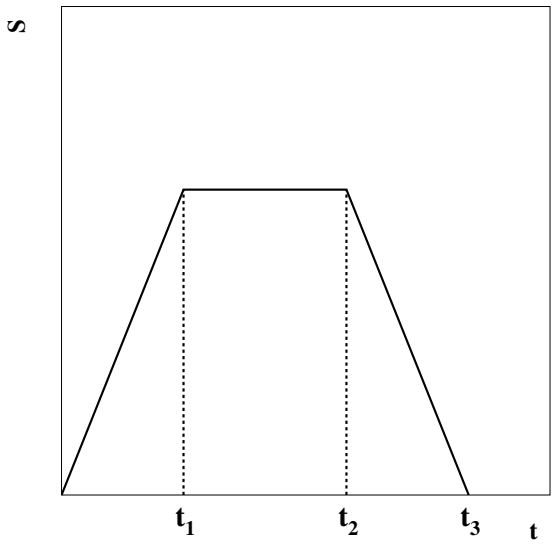

Figure B1. A schematic view of variation in time of the emission area on the jaw surface covered by the electric field of a bunch (in arbitrary units).

APPENDIX B. THE SIZE OF EMISSION AREA

Here we derive the formula for calculating N_e, see Eq. (32). Figure B1 shows schematically how the emission area varies over time as a bunch passes through the collimator. Because of a step-like form of the field, the electric field of the bunch covers only a part of the jaw surface. For that reason,

$$\mathrm{d}x \int \Theta(z,t)\mathrm{d}z\mathrm{d}t = \int S(t)\mathrm{d}t, \tag{B1}$$

where $\Theta(z,t) = \Big[\theta(z-\beta ct) - \theta(z-\beta ct - L_b)\Big]$.

There are three time stages: $[0,t_1]$: $S(t) = \delta s \cdot t/t_1$; $[t_1,t_2]$: $S(t) = \delta s$; $[t_2,t_3]$: $S(t) = \delta s \cdot [1-(t-t_2)/(t_3-t_2)]$, with $\delta s = \mathrm{d}x \cdot L_b$. Therefore, $\int S(t)\mathrm{d}t = \delta s \cdot t_2$, with $t_2 = L_j/c$. With these substitutions, Eq. (32) finally becomes

$$N_e(\beta_{FN}) = n_b N_r \frac{L_b L_j}{c} \sum \frac{2}{e} \int_0^\infty \mathbf{J}(\beta_{FN} E_y(x, \bar{\delta_y}))\mathrm{d}x. \tag{B2}$$

REFERENCES

1. Wiedemann, H., *Particle Accelerator Physics*, Springer, Berlin-Heidelberg, Germany, 2007.
2. Levchenko, B. B., "Modification of relativistic beam fields under the influence of external conducting and ferromagnetic flat boundaries," *Prog. Theor. Exp. Phys.*, Vol. 2020, No. 1, 013G01–013G29, 2020.
3. Thomson, W., "On electrical images," *Report of the Seventeenth Meeting of the British Association for the Advancement of Science*, Vol. 1, Part II, 6, London, 1848.
4. Maxwell, J. C., *A Treatise on Electricity and Magnetism*, Vol. 1, Ch. 11, The Calendon Press, Oxford, 1873.
5. Laslett, L. J., "On intensity limitations imposed by transverse space-charge effects in circular particle accelerators," *Proc. BNL Summer Study on Storage Rings*, 324–363, BNL-7534, 1963.
6. Chao, A. W., *Physics of Collective Beam Instabilities in High-energy Accelerators*, John Wiley and Sons, New York, 1993.
7. Hofmann, A., "Tune shifts from selffields and images," *Proceedings of the 5th General Accelerator Physics Course*, Vol. 1, CERN-94-01, Jyväskylä, Finland, 1992.
8. Levchenko, B. B., "Electric and magnetic fields generated by a charged bunch between parallel conducting plates," *Physics Research International*, Vol. 2010, 201730–201735, 2010.
9. Brüning, O., P. Collier, P. Lebrun, S. Myers, R. Ostojic, J. Poole, and P. Proudlock, *LHC Design Report. The LHC Main Ring*, Vol. 1, CERN, Geneva, 2004.
10. Apollinari, G., I. B. Alonso, O. Brüning, P. Fessia, M. Lamont, L. Rossi, and L. Tavian, *High-luminosity Large Hadron Collider (HL-LHC)*, Vol. 4, CERN-2017-007-M, CERN, Geneva, 2017.
11. "Report reveals full reach of LHC programme," *CERN Courier*, Vol. 59, 9, 2019, https://cerncourier.com/a/report-reveals-full-reach-of-lhc-programme.
12. Smythe, W. R., *Static and Dynamic Electricity*, McGraw-Hill Book Company, New York, 1950.
13. Zotter, B., "The Q-shift of off-center particle beams in elliptic vacuum chambers," *Nucl. Instrum. Meth.*, Vol. 129, 377–395, 1975.
14. Cimino, R., I. R. Collins, M. A. Furman, M. Pivi, F. Ruggiero, G. Rumolo, and F. Zimmermann, "Can low energy electrons affect high energy physics accelerators?," *Phys. Rev. Lett.*, Vol. 93, 014801, 2004.
15. Fowler, R. H. and L. W. Nordheim, "Electron emission in intense electric fields," *Proc. Roy. Soc. (London)*, Vol. A119, 173–181, 1928.
16. Nordheim, L. W., "The effect of the image force on the emission an reflexion of electrons by metals," *Proc. Roy. Soc. (London)*, Vol. A121, 626–639, 1928.
17. Nordheim, L., "Die theorie der electronenemission der metalle," *Physikalische Zeitschrift*, Vol. 30, No. 7, 117–196, 1929.

18. Elinson, M. I. and G. F. Vasil'ev, *Field Emission*, Fizmatgiz, Moscow, 1958 [in Russian].
19. Fursey, G., *Field Emission in Vacuum Microelectronics*, Kluwer Academic Plenum Publishers, New York, 2005.
20. Sommerfeld, A. and H. Bethe, *Elektronentheorie der Metalle*, Springer, Berlin, 1967.
21. Murphy, E. L. and R. H. Good, Jr., "Thermionic emission, field emission and the transition region," *Phys. Rev.*, Vol. 102, No. 6, 1464–1473, 1956.
22. Christov, S. G., "Recent test and new applications of the unified theory of electron emission," *Surf. Sci.*, Vol. 70, 32–51, 1978.
23. Good, R. H., Jr. and E. W. Müller, "Field emission," *Encyclopedia of Physics*, Vol. XXI, S. Flügge (Ed.), 1956.
24. Shrednik, V. N., "The theory of field emission from metals," *Cold Cathodes*, M. I. Elinson (Ed.), Sovetskoe Radio, Moscow, 1974 [in Russian].
25. Gomer, R., *Field Emission and Field Ionization*, AIP, New York, 1993.
26. Modinos, A., *Field, Thermionic, and Secondary Electron Emission Spectroscopy*, Plenum Press, New York, 1983.
27. Eidelman, S., et al., "Review of particle physics," *Phys. Lett.*, Vol. B592, Nos. 1–4, 1–5, 2004.
28. Burgess, R. E., H. Kroemer, and J. M. Houston, "Corrected values of Fowler-Nordheim field emission function $\theta(y)$ and $S(y)$," *Phys. Rev.*, Vol. 90, 515, 1953.